NeuroImage 42 (2008) 19–27

Contents lists available at ScienceDirect

NeuroImage

journal homepage: www.elsevier.com/locate/ynimg

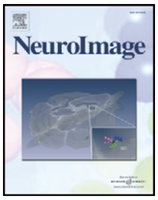

Longitudinal neuroanatomical changes determined by deformation-based morphometry in a mouse model of Alzheimer's disease

Jonathan C. Lau [a], Jason P. Lerch [a,b], John G. Sled [b], R. Mark Henkelman [b], Alan C. Evans [a], Barry J. Bedell [a,*]

[a] *McConnell Brain Imaging Centre, Montreal Neurological Institute, McGill University, 3801 University Street, Montreal, QC, Canada H3A 2B4*
[b] *Mouse Imaging Centre, Hospital for Sick Children, 555 University Avenue, Toronto, Ontario, Canada M5G 1X8*

ARTICLE INFO

Article history:
Received 27 December 2007
Revised 18 April 2008
Accepted 20 April 2008
Available online 7 May 2008

ABSTRACT

Magnetic resonance imaging (MRI) of transgenic mice has the potential to provide valuable insight into the complex mechanisms underlying Alzheimer's disease (AD). Quantification of pathological changes is typically performed using manual segmentation methods, and requires *a priori* hypotheses about anatomical structures for volumetric measurement. Alternatively, deformation-based morphometry (DBM) has been shown to be a powerful, automated technique for detecting anatomical differences between populations by examining the deformation fields used to nonlinearly warp MR images. In this multiple timepoint, *in vivo* study, we have applied an automated, unbiased technique for the creation of a nonlinear, population-specific reference space from which robust DBM analysis can be performed. A general, linear mixed-effects model framework was developed to follow the evolution of structural changes in mouse brain from 2.5 to 9 months of age, and to examine neuroanatomical differences between a transgenic (TG) APP/PS1 murine model of AD and wild-type (WT) littermates. Morphometric abnormalities in the TG group were localized to regions of the hippocampus, cortex, olfactory bulbs, stria terminalis, brain stem, cerebellum, and ventricles. Although volumetric reductions were detected in TG mice, no general brain atrophy was found, suggesting a developmental, rather than a degenerative, pathological process. Finally, we established a strong correlation between a DBM summary measure and manually segmented volumes for each image in the dataset. These results support the utility of DBM to study longitudinal morphological changes in mouse models of central nervous system diseases in an automated and exploratory fashion.

Introduction

Alzheimer's disease (AD) is a devastating neurodegenerative disease that currently afflicts over 4.5 million people in the U.S., and which is predicted to rise to 11.3–16 million by 2050 (Hebert et al., 2003). This staggering prevalence and rapidly growing incidence point to the desperate need for the development of new therapeutic avenues for the treatment of AD. While currently available drugs provide limited, short-term, symptomatic effects, drug development has moved toward disease-modifying therapies which would slow, reverse, or ultimately prevent AD. These disease-modifying agents are generally designed for molecular targets known to be involved in the pathogenesis of AD. However, the ultimate phenotypic consequences of the expression of these molecular targets remain poorly understood.

Longitudinal, anatomical magnetic resonance imaging (MRI) studies provide a non-invasive means of following the subtle structural changes which occur during the natural evolution of AD (Lerch et al., 2005). While most quantitative MRI studies of AD-related neuroanatomical alterations have focused on human subjects (Anderson et al., 2005; Barnes et al., 2007; Thompson et al., 2007), a few recent studies have examined volumetric changes in transgenic (TG) mouse models of AD (Redwine et al., 2003; Delatour et al., 2006; Oberg et al., in press). TG murine models with targeted expression of mutated amyloid precursor protein (APP) genes demonstrate many of the cognitive (Palop et al., 2003) and neuropathological features of AD, including senile plaques, neuronal impairments, acetylcholine (ACh) denervation (Hsia et al., 1999; Mucke et al., 2000; Aucoin et al., 2005), cerebral hypometabolism (Niwa et al., 2002), and alterations in synaptic transmission (Larson et al., 1999). These models are particularly useful for studying the natural evolution of AD, as well as for evaluation of the therapeutic efficacy of new disease-modifying agents.

Quantitative anatomical MRI studies of TG models of AD have largely been limited to manual segmentation of regions-of-interest (ROIs) (Redwine et al., 2003; Delatour et al., 2006;

---

* Corresponding author. McConnell Brain Imaging Centre, Montreal Neurological Institute, 3801 University St., BT-209, Montreal, Quebec, Canada H3A 2B4. Fax: +1 514 398 8948.
E-mail address: bbedell@bic.mni.mcgill.ca (B.J. Bedell).

1053-8119/$ – see front matter © 2008 Elsevier Inc. All rights reserved.
doi:10.1016/j.neuroimage.2008.04.252

Oberg et al., in press). These techniques, however, are labour-intensive, prone to intra- and inter-rater bias, relatively insensitive to subtle morphological brain changes (Ashburner et al., 2003), and require *a priori* hypotheses about affected anatomical structures, thereby excluding potentially relevant regions from the analysis.

In order to overcome these inherent limitations, we have developed an alternative, automated approach, using deformation-based morphometry (DBM), to detect the natural evolution of neuroanatomical changes in TG mouse models of AD. DBM is a quantitative image analysis technique which evaluates information contained within the vector field generated by the nonlinear warping of an individual MRI scan to a reference template (Davatzikos et al., 1996; Bookstein, 1997; Thompson and Toga, 1997; Ashburner et al., 1998; Cao and Worsley, 1999; Chung et al., 2001). In contrast to voxel-based morphometry (VBM) (Ashburner and Friston, 2000; Good et al., 2001; Bookstein, 2001; Ashburner and Friston, 2001), DBM does not require segmentation of the brain into different tissue compartments, which can be particularly challenging in the murine brain. Further, DBM has been successfully applied to examine cross-sectional morphological differences and longitudinal anatomical changes in human (Fox et al., 2001; Janke et al., 2001; Studholme et al., 2004; Leow et al., 2006) and, more recently, mouse neuroimaging studies (Verma et al., 2005; Zhang et al., 2005; Chen et al., 2006; Nieman et al., 2006; Spring et al., 2007). While the majority of DBM studies of mouse brains have been limited to cross-sectional or dual timepoint studies, Verma et al. (Verma et al., 2005) and Zhang et al. (Zhang et al., 2005) recently extended this technique to study murine brain development over multiple timepoints, comparing changes in diffusion-tensor MR images of fixed, *ex vivo* brains between post-natal developmental stages using qualitative, landmark based and ROI-based quantitative measures.

In the present study, we have utilized DBM to examine *in vivo* neuroanatomical differences between TG mouse models of AD and wild-type (WT) littermates, as well as follow the evolution of these structural changes from 2.5 to 9 months of age using a general, linear-model framework based on the deformation maps. The relationship between the results of our automated analysis and conventional manual segmentation methods was assessed for a number of different anatomical structures. This fully-automated framework allows for voxelwise statistical analysis and obviates the need to specify pre-determined ROIs, thereby resulting in an unbiased, exploratory method for analyzing subtle differences between TG and WT populations.

Materials and methods

Animals and MRI measurements

MRI scans were kindly provided by AstraZeneca R&D (AstraZeneca, Södertälje, Sweden). The mouse models and MRI scanning protocols used for these studies have previously been described, in detail, by Oberg et al. (Oberg et al., in press). Briefly, 20 TG APP/PS1 mice (11 females, 9 males) and 13 WT littermates (11 females, 2 males) were scanned at 2.5 months (14 TG, 9 WT), 4.5 months (13 WT, 9 WT), 6.5 months (10 TG, 10 WT), and 9 months (8 TG, 13 WT) of age for a total of 86 scans. MRI scans were performed using a horizontal-bore 9.4 T magnet (Bruker BioSpec 94/30, Bruker, Ettlingen, Germany) equipped with a 12 cm inner-diameter self-shielded gradient system (maximum gradient strength 400 mTm^{-1}). A 72-mm volume coil was used for excitation and a quadrature mouse brain surface coil (Bruker, Germany) was used for signal detection. MR images were acquired with a 3D inversion-recovery, spin-echo sequence with the following scan parameters: matrix size = 128 × 128 × 64, FOV = 2.0 cm × 2.0 cm × 1.0 cm, resolution = 156.25 μm × 156.25 μm × 156.25 μm, TR = 2500 ms, TE = 5.7 ms, RARE factor = 4, inversion delay = 500 ms, and NEX = 1. The total acquisition time was 1 h and 26 min.

Longitudinal deformation-based morphometry

Reference model and nonlinear registration

Image processing was performed using software available from the McConnell Brain Imaging Centre (http://www.bic.mni.mcgill.ca/software) at the Montreal Neurological Institute (Montreal, Canada). A single, average MRI reference space was generated using all 86 scans following the methods of Kovacevic et al. (Kovacevic et al., 2005). A representative scan was chosen as the prior model for initializing the reference model creation algorithm. The brain region of the representative scan was manually outlined using the Display software package (Montreal Neurological Institute, Montreal, Canada) yielding a brain mask for our initial model space. This brain mask was used for all subsequent reference model creation steps. Briefly, each scan was first registered using a rigid body (lsq6) transformation to the prior model (Collins et al., 1994). Next, images were corrected for intensity nonuniformity artifacts using the N3 algorithm (Sled et al., 1998) with nonuniformity correction limited to the brain-masked region of the model. The specific parameters utilized were: distance = 8 mm, FWHM = 0.15 mm, number of iterations = 100, and number of runs = 8. Pairwise 12-parameter (lsq12) registrations were then performed to create an unbiased affine average model of the entire dataset. This transformation was followed by a series of nonlinear registration steps, applied in a coarse-to-fine fashion, with each subsequent step using the best previous model as a registration target (Collins et al., 1995; Kovacevic et al., 2005). After concatenating the sequential transformations, the scans were resampled and averaged, resulting in a population-specific model. The registration parameters are provided in Table 1.

The resulting deformation field, consisting of 200 μm grid points, was inverted. The linear terms were removed and the deformation field was centered to the average displacement across the entire population studied, allowing for the vector fields to be interpreted in a reference space. After resampling, the final deformation field provided a nonlinear mapping, $\mathbf{T(x)}$, from reference space to the native space of each scan at every voxel, $\mathbf{x}$.

Assessment of registration performance

Inaccuracies in reference model creation can occur due to warping to a finite voxel size (quantization) and imperfect/suboptimal calculation of the nonlinear transformation. In order to assess the registration performance of the reference model creation process, we utilized manual segmentation data for three neuroanatomical structures (whole brain, hippocampus, and lateral ventricles) that had been segmented in the native space of all 86 scans used in the study. The manual segmentations of these three structures were provided by AstraZeneca R&D (AstraZeneca, Södertälje, Sweden). The segmentation methods have been described, in detail, by Lavebratt et al. (Lavebratt et al., 2006) and Oberg et al. (Oberg

Table 1
Registration schedule

Step	FWHM (μm)	Filter type	Grid resolution (μm)
lsq6	5000	Gaussian	NA
lsq6	2000	Gaussian	NA
lsq6	1000	Gradient	NA
lsq6	800	Gaussian	NA
lsq6	500	Gaussian	NA
lsq12	800	Gaussian	NA
lsq12	600	Gradient	NA
lsq12	400	Gaussian	NA
nlin1	800	Gaussian	1000
nlin2	600	Gaussian	800
nlin3	500	Gaussian	700
nlin4	400	Gaussian	600
nlin5	400	Gaussian	400
nlin6	300	Gaussian	400
nlin7	200	Gaussian	300
nlin8	200	Gaussian	200

NA = not applicable.

et al., in press). The manual segmentations of each MRI scan were run through an iterative loop as follows:

1. identify forward transformation between native space and reference space;
2. apply transformation to native structure segmentation to obtain a resampled segmentation in reference space.

A voxel overlap index was then calculated across all scans for each manually segmented structure. In principle, the reference space segmentations obtained from each scan should be identical. However, the aforementioned practical factors, as well as potential rater variation in the manual segmentation, may cause a mismatch at the structure border especially for low-dimensional transformations. The voxel overlap index was therefore assessed at progressively decreasing spatial resolution as follows:

1. every voxel in reference space was assigned a value between 0 and 100% (perfect overlap) for a given structure, corresponding to the proportion of the 86 scans for which that voxel included that structure;
2. maximal perfect overlap was defined as the peak number of voxels exhibiting perfect overlap across all registration stages;
3. a voxel overlap metric was computed according to the method utilized by Spring et al. (Spring et al., 2007), specifically:

$$\text{voxel overlap} = \frac{\text{voxels at stage with perfect overlap}}{\text{voxels at stage with maximal perfect overlap}} \tag{1}$$

Adaptive spatial filtering

In order to reduce noise in the deformation maps, we applied the intensity consistent approach described by Studholme et al. (Studholme et al., 2003; Studholme et al., 2004). This anisotropic filter was selected over more traditional Gaussian smoothing methods since it is edge-preserving and, thus, better respects anatomical boundaries. Briefly, this algorithm performs a Gaussian blur, $f(\mathbf{k})$, at each voxel, $\mathbf{x}$, of the associated deformation field, where the contribution of each kernel neighbor, $\mathbf{k} \in K$, depends on the MR intensity-based statistical relationship, $p_{xk}(\mathbf{x},\mathbf{x}\text{-}\mathbf{k})$ between $\mathbf{x}$ and its relative neighbor $\mathbf{x}\text{-}\mathbf{k}$. The value of $p_{xk}(\mathbf{x},\mathbf{x}\text{-}\mathbf{k})$ was computed from an estimate of the conditional probability of the average and individual subject scan intensity within the local neighborhood, K (Studholme et al., 2003). The filtering equation can be formalized as

$$\tilde{\mathrm{T}}(\mathbf{x}) = \frac{1}{\boldsymbol{\Theta}(\mathbf{x})} \int_{k\in K} \mathrm{T}(\mathbf{x}-\mathbf{k}) \cdot f(\mathbf{k}) \cdot p_{xk}(\mathbf{x}, \mathbf{x}-\mathbf{k}) \cdot d\mathbf{k} \tag{2}$$

In order to account for the variable contribution of neighbors at each voxel,

$$\boldsymbol{\Theta}(\mathbf{x}) = \int_{\mathbf{k}\in K} f(\mathbf{k}) \cdot p_{xk}(\mathbf{x}, \mathbf{x}-\mathbf{k}) \cdot d\mathbf{k} \tag{3}$$

was computed and used to normalize the local volume. A kernel width of 1.0 mm was used for filtering.

Computation of the Jacobian determinant

In order to examine the local volume change in each subject, the Jacobian determinant (or simply the Jacobian), $\tilde{\boldsymbol{J}}(\mathbf{x})$, for each vector, $\tilde{\boldsymbol{T}}(\mathbf{x})$, in the filtered deformation field was computed at every voxel (Chung et al., 2001; Janke et al., 2001). This metric has been shown to provide a simple and direct means of determining local, voxelwise expansion or compression relative to the reference space. Global effects of size were reintroduced at every voxel by multiplying the local Jacobian by the scale term associated with the spatial linear normalization of each image to the reference space. The scaled Jacobian was log-transformed in order to better approximate a symmetric normal distribution, thereby permitting the use of a mixed-effects model.

Longitudinal statistical analysis of the voxelwise Jacobian

In order to characterize the local trajectory of change, mixed-effects models were tested at every voxel within the brain from the filtered, Jacobian maps. Mixed-effect models extend standard linear models by adding an additional error term that corresponds to the variable intercept for each subject in a longitudinal dataset with no requirement of balance in the data (i.e. it is not necessary for all mice to have the same number of scans) (Pinheiro and Bates, 2002). The nature of the Jacobian's relationship with age was modeled as a sum of fixed and linear components, and different polynomial models were evaluated for the developmental trajectory. Interactions with genotype and sex were assessed, and to account for within-subject dependencies, random effects for both intercept and slope for each individual were tested. For this analysis, age was centered to the mean age of the population. Finally, mixed-effects models were compared using voxelwise likelihood ratio tests, and the simpler model was chosen whenever it was found to explain most of the variance.

The resulting statistical maps were corrected for multiple comparisons using the false discovery rate (FDR) procedure with $q = 0.05$ (Genovese et al., 2002). A single FDR threshold was determined by pooling the uncorrected P-values across all effects and all voxels tested. By taking into account the degrees of freedom for a given statistical test, a t-value threshold for each statistical map was computed from the FDR-determined P-value. Regions of significant group-dependent deformation were reported with the aid of a mouse atlas (Paxinos and Franklin, 2001). All statistical analyses were performed using the R software package (www.r-project.org) in conjunction with the nlme and RMINC libraries.

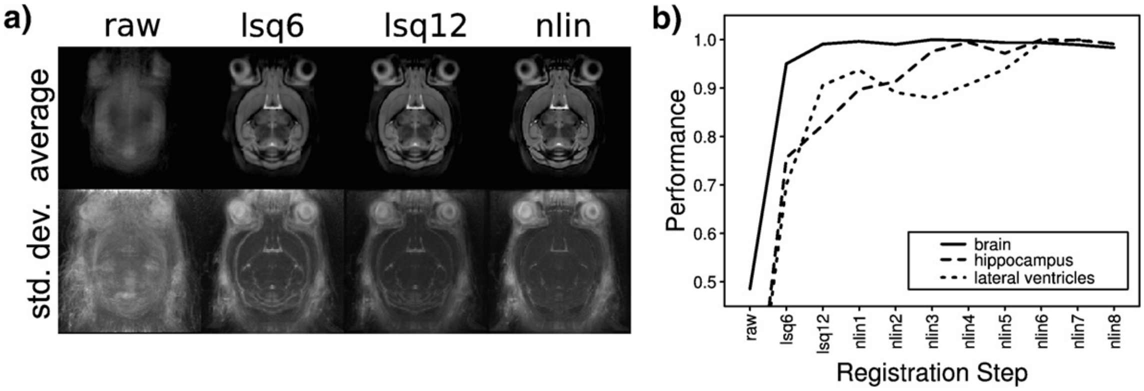

Fig. 1. Pipeline results for successive stages of reference creation. (a) Average and standard deviation images of the same transverse slice at successive stages of registration. (b) Plots of performance (quantified as voxel overlap) versus registration step for each manually segmented scan. Note that the performance of the algorithm is seen to plateau after the sixth nonlinear registration step.

Relationship between DBM results and conventional manual volumetry

In order to examine the relationship between the automated results from DBM and manual volumetric analyses, we studied the longitudinal patterns of change in manual segmentations of whole brain, hippocampus, and lateral ventricles using mixed-model regression. We evaluated registration performance across all 86 subjects studied. These segmentations were used to assess the same mixed-effects components as in the longitudinal statistical analysis for DBM.

We examined the relationship between an automated measure of volume computed from the nonlinear transformations and the manually segmented volumes for all 86 scans. The volume of interest for each structure was derived from the probabilistic average of all individual manual segmentations, thresholding the 3D probability map at 50% and manually correcting the borders. Subsequently, these reference masks for each structure were transformed back into the native space of each scan using the previously computed nonlinear transformations, thereby providing an automated estimate of the actual volume. The correlation between the automated volume and the manually segmented volume for each scan and structure was then determined.

Results

Reference model and nonlinear registration

Prior to the DBM analysis, the quality of registration was assessed in order to ensure that reference creation had been properly performed. Fig. 1a depicts the qualitative improvements that can be observed over the course of reference model creation. The variability of neuroanatomical features decreased with pipeline progression, particularly in white matter structures (e.g. the cerebellar and dorsal hippocampal commissures), and the ventricles. The extra-axial tissues remained highly variable since they were excluded from the registration steps. Fig. 1b shows the quantitative improvement using our voxel overlap metric. Improvements were observed to plateau following six generations of nonlinear registration.

Results of longitudinal DBM analysis

The voxelwise, log-transformed Jacobian provides a biologically interpretable measure of local volumetric expansion (>0) or compression (<0) relative to the reference space. Mixed-effects models were tested and compared across all voxels in the brain using ANOVA. We tested main effects of

Table 2
Main effects of genotype

Region	Symmetry	β_1	*t*-value	β_1 greater in
Primary somatosensory cortex (jaw region)	right	0.088	4.93	WT
Primary somatosensory cortex (barrel field)	bilateral	0.126	5.11	WT
Retrosplenial and cingulate cortex	medial	0.155	6.58	WT
Piriform cortex	left	0.100	5.03	WT
Olfactory bulb	bilateral	0.126	6.07	WT
Paraflocculus	bilateral	0.116	4.87	WT
Anterior commissure	bilateral	0.146	5.83	WT
Corpus callosum	bilateral	0.172	6.20	WT
Cingulum/Dorsal hippocampal commissure	bilateral	0.191	5.69	WT
Cerebellar commissure	bilateral	0.181	5.31	WT
Bed nucleus of stria terminalis	bilateral	−0.170	−8.21	TG
Dorsal superior colliculus	bilateral	−0.116	−5.68	TG
Dorsal periaqueductal gray matter	bilateral	−0.062	−3.56	TG
Stria terminalis	bilateral	−0.175	−4.39	TG
Brachium of superior colliculus	bilateral	−0.097	−3.66	TG
Lateral ventricles	bilateral	−0.137	−5.97	TG
Third ventricle	medial	−0.103	−3.52	TG

β_1 = fixed-effect for genotype.

Table 3
Interactions between age and genotype

Region	Symmetry	β_3	*t*-value	β_3 greater in
Lateral entorhinal cortex	left	0.057	3.93	WT
Retrosplenial granular b cortex	medial	0.049	3.75	WT
Hippocampus: CA3 and GrDG	bilateral	0.030	3.95	WT
Flocculus/Paraflocculus	bilateral	0.028	3.44	WT
Primary somatosensory cortex (jaw region)	bilateral	−0.016	−3.88	TG
Primary somatosensory cortex (barrel field)	left	−0.026	−4.09	TG
Retrosplenial and cingulate cortex	right	−0.016	−3.56	TG
Piriform cortex	bilateral	−0.015	−5.02	TG
Dorsolateral hippocampus (CA1 to CA2)	bilateral	−0.032	−4.94	TG
Septofimbrial and septal nucleus	left	−0.017	−6.06	TG
Lateral globus pallidus	right	−0.024	−4.33	TG
Ventral posterolateral thalamic nucleus	left	−0.012	−4.12	TG
Medial vestibular nucleus	bilateral	−0.010	−4.02	TG
Cingulum/Dorsal hippocampal commissure	left	−0.041	−6.43	TG
Cerebellar commissure	right	−0.022	−4.76	TG
Lateral ventricles	bilateral	−0.017	−4.67	TG
Third ventricle	medial	−0.018	−4.49	TG

β_3 = interaction between age and genotype.

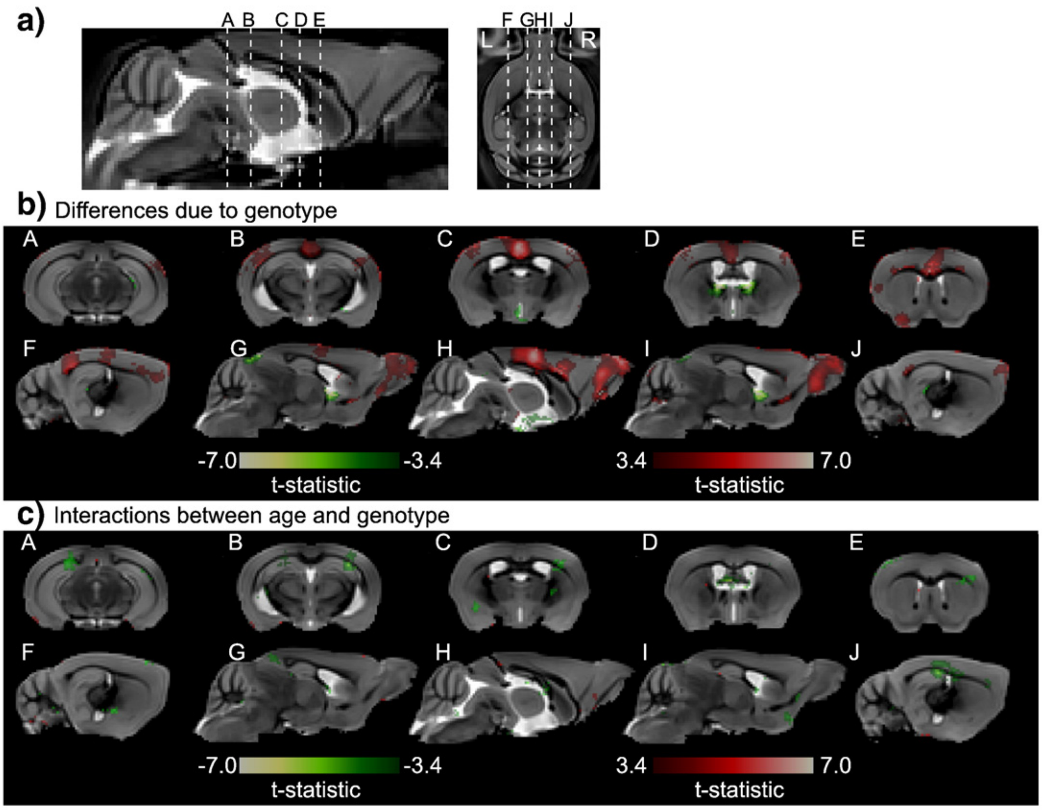

Fig. 2. Statistical maps demonstrating local volume differences between TG and WT populations. (a) The positions of representative slices throughout the reference space are marked with dashed lines in a mid-sagittal slice for the coronal sections (A-E) and a mid-transverse slice for the sagittal sections (F-J). (b) Regions demonstrating volumetric differences due to genotype across all timepoints. Volumetric expansion and reduction in TG versus WT are shown in green and red, respectively. (c) Regions demonstrating dynamic interactions between age and genotype. Positive and negative interactions are shown in green and red, respectively. All coloured regions are statistically significant by pooled FDR ($q=0.05$).

gender, as well as interactions of gender with age and genotype. However, the inclusion of these terms did not result in any significant effects in the analysis. As such, the final statistical model included fixed-effects for genotype (β_1), age (β_2), and the interaction of genotype with age (β_3), as well as a random intercept to account for within-subject variability (b_i). This

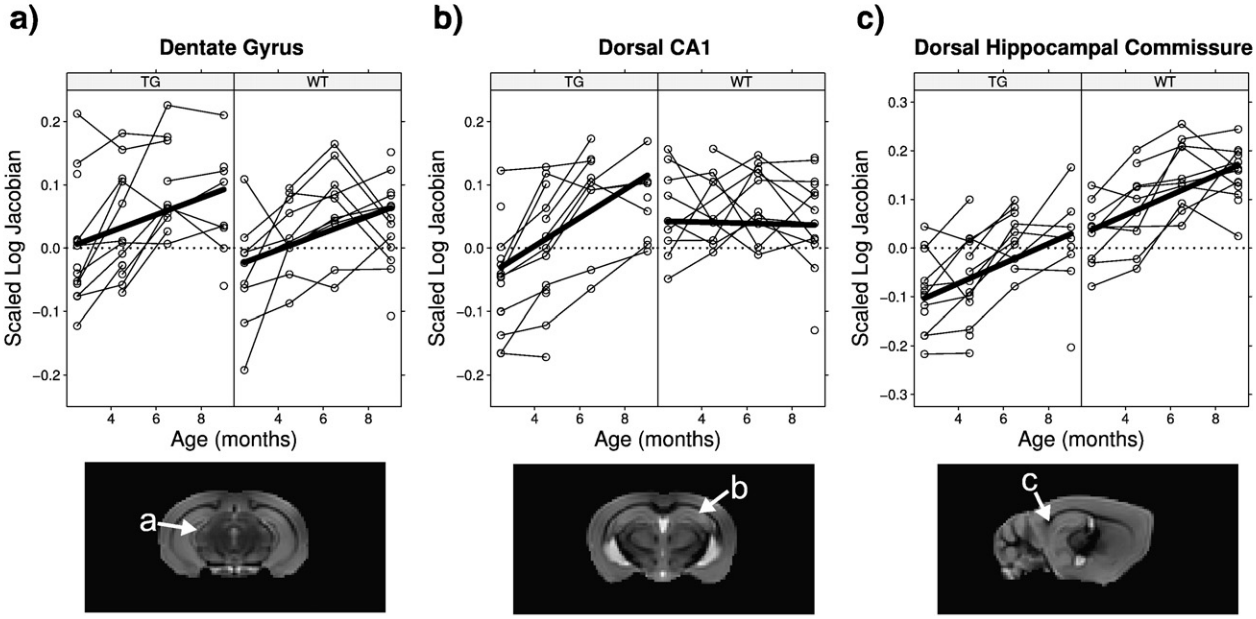

Fig. 3. Dynamic longitudinal changes illustrated within the hippocampus using the local scaled Jacobian. The voxelwise scaled Jacobians are plotted as open circles. The final predicted model, represented by a thick solid line, includes only significant components of the mixed-effects model, and individual trajectories are connected by thin solid lines. Regions in (a) the left lateral dentate gyrus, (b) the right dorsal hippocampus within CA1, and (c) the left dorsal hippocampal commissure are shown.

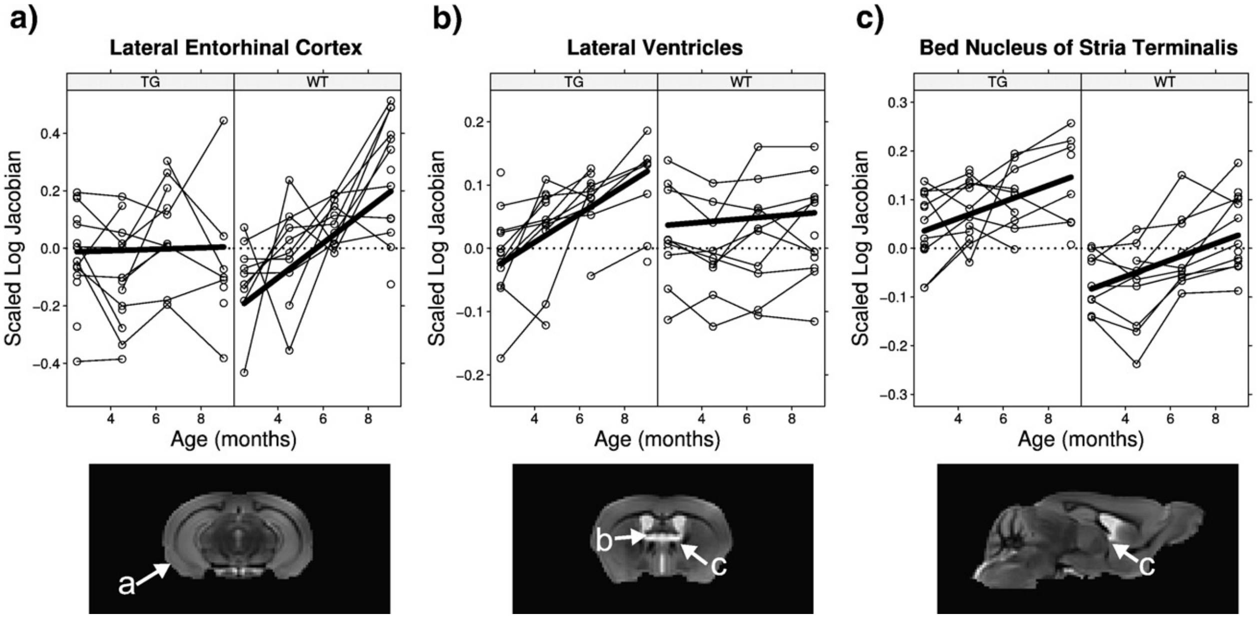

Fig. 4. Dynamic longitudinal changes illustrated for several regions throughout the brain. The voxelwise scaled Jacobians are plotted as open circles. The final predicted model, represented by a thick solid line, includes only significant components of the mixed-effects model, and individual trajectories are connected by thin solid lines. Regions of (a) the left lateral entorhinal cortex, (b) the lateral ventricles, and (c) the bed nucleus of the stria terminalis are shown.

simple model was found to be as robust as more complicated models (e.g. modeling both slope and intercept as random effects). Thus, for each subject *i*, the model evaluated was

$$J_i(\mathrm{x}) = \beta_0 + b_i + \beta_1 \times \text{genotype} + \beta_2 \times \text{ age} + \beta_3 \times \text{ age} \times \text{genotype} + \epsilon \quad (4)$$

where β_0 represents the intercept term and ϵ is the residual error in the model. The results from the analysis showed significant patterns of local shape change that can be described on the basis of these underlying model components. Each component provides different information about local shape change. A significant age term is an indicator of local volume growth or loss with genotype effects removed. A significant genotype term indicates regions demonstrating inherent genetic differences between groups, in particular, where WT is larger than TG (reduction) and where TG is larger than WT (expansion) with age effects removed. Finally, a significant interaction between genotype and age signifies a region affected differently by aging in each groups. This interaction component is dependent on the values of both the age and genotype terms, and, thus, the direction of change was interpreted on a region-by-region basis.

Significant growth for both groups of animals was detected throughout the brain, particularly in the hippocampus, olfactory bulbs, thalamus, cerebellar commissure, ventricles, and white matter tracts (e.g. anterior commissure and corpus callosum). Significant volume reduction was noted in several cortical regions (entorhinal, piriform, somatosensory), as well as in the caudate.

Neuroanatomical regions displaying significant genetic differences in volume are summarized in Table 2 for simple differences related to genotype and Table 3 for more complex, dynamic interactions between age and genotype. No interactions with sex were observed in the population studied. Representative regions of significant morphological change or difference are shown in Fig. 2. The dynamics of longitudinal change are illustrated using voxelwise regression plots at

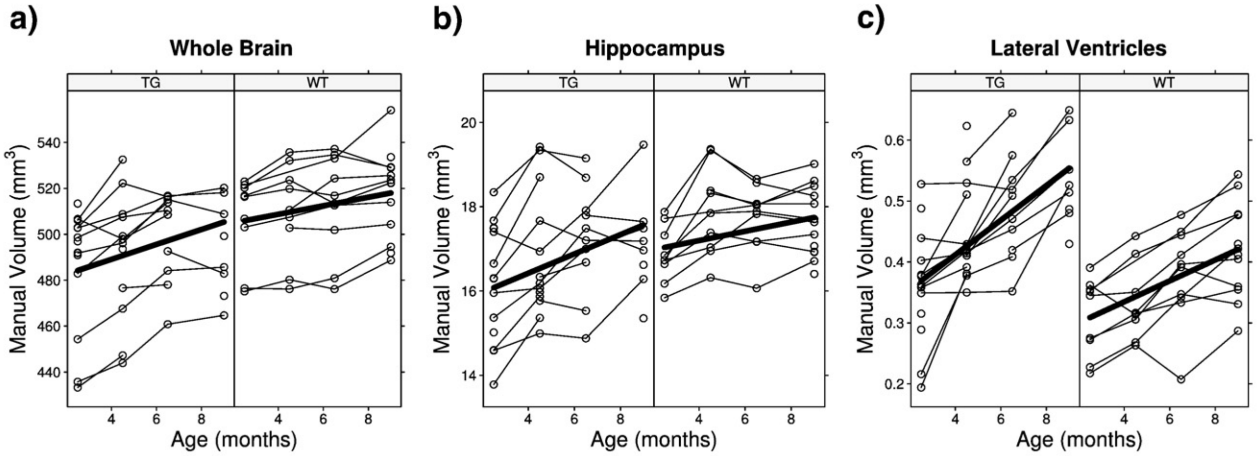

Fig. 5. Mixed-effects regression plots in three manually segmented neuroanatomical volumes: (a) whole brain, (b) hippocampus, and (c) lateral ventricles. The raw datapoints are plotted as open circles. The final predicted curve is represented by a solid line, and individual trajectories are connected by thin solid lines.

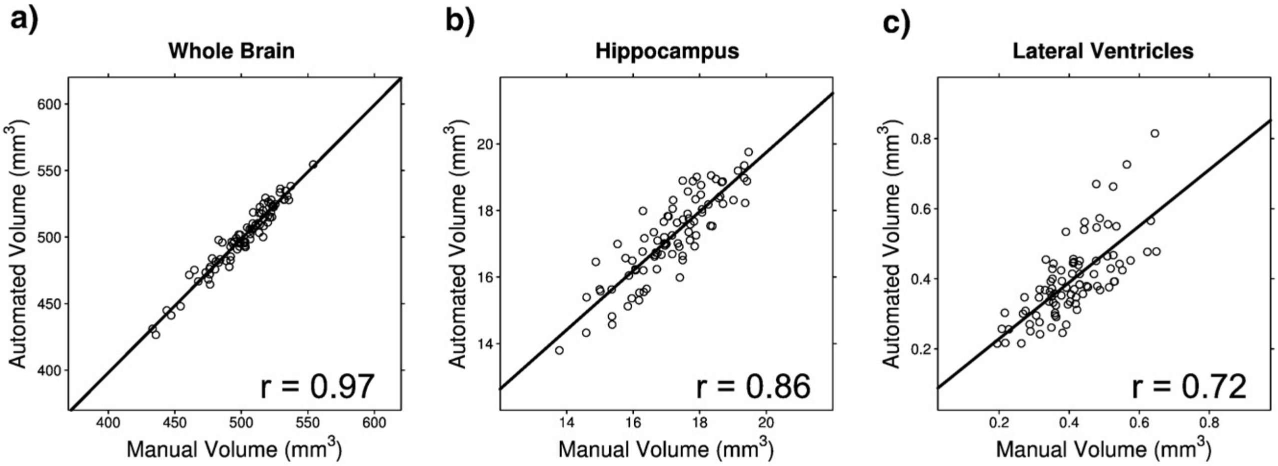

Fig. 6. Correlation between automated and conventional manual segmentations of (a) whole brain, (b) hippocampus, and (c) lateral ventricles.

specific, significant individual voxels of the hippocampus and other brain structures (entorhinal cortex, lateral ventricles, bed nucleus of the stria terminalis) in Figs. 3 and 4, respectively.

Longitudinal findings from manual segmentations

While Figs. 3 and 4 demonstrate the results of the automated voxel-based analysis, we also assessed the temporal dynamics for larger structures using the manual segmentation data. The best-fit, mixed-effects regression plots for each of the manually segmented structures, specifically whole brain, hippocampus and lateral ventricles, are shown in Fig. 5. All three structures exhibited significant linear growth ($P<0.0001$).

Differences due to genotype (TG versus WT) were found in all three manually segmented structures. In TG mice, whole brain and hippocampus demonstrated reduced volume, while the lateral ventricles showed enlarged volume relative to WT. Significant interactions between age and genotype components in the hippocampus and lateral ventricles, and marginal interactions in the whole brain measure ($P=0.054$) suggested an additional dynamic difference between groups that varied with age.

Correlation between automated and manually segmented measures

The correlation plots between the automated and manually segmented volumes for whole brain ($r=0.97$; $P<0.0001$), hippocampus ($r=0.86$; $P<0.0001$) and lateral ventricles ($r=0.72$; $P<0.0001$) are shown in Fig. 6. While still highly significant, the lateral ventricles demonstrated the greatest variability in the correlation plot (Fig. 6c).

Discussion

In this work, we have examined morphological changes and differences in a longitudinal anatomical MRI study of TG APP/PS1 mice and WT littermates using DBM. The analysis was performed using a unified, population-specific reference space and mixed-effects modeling to allow for a voxelwise study of the distribution of age-related volumetric changes and regional differences related to genotype (i.e. TG vs. WT).

We found strong, positive correlations between results computed using our automated methods and manual segmentation/volumetry in selected anatomical structures for all 86 scans (see Fig. 6). However, small offsets are evident in Figs. 6b and c, indicating a systematic bias inherent in the automated method. Not surprisingly, this bias becomes more evident as the size of the segmented structure decreases, with the greatest deviations observed in the lateral ventricles (see numerical scales on the axes of the plots in Fig. 6). Nevertheless, the highly significant correlation analysis ($P<0.0001$) justifies the use of reproducible, automated segmentation rather than manual approaches that suffer from intra-/inter-rater variability.

While a range of different longitudinal patterns were observed throughout the brain, emphasizing the heterogeneous nature of neuroanatomical changes, a number of distinct patterns identified in this study were particularly interesting. Growth with age was identified in the hippocampus, olfactory bulbs, thalamus, ventricles, cerebellar commissure, and white matter tracts in both TG and WT groups. On the other hand, age-related volume loss was identified in the lateral entorhinal, piriform, and somatosensory cortices, as well as the caudate nucleus.

A number of expected and unexpected findings were discovered upon examining genotypic differences. Volume reduction was observed in the cingulate, retrosplenial, and primary somatosensory cortices of TG mice relative to their WT littermates. Substantial β-amyloid pathology has been shown in these regions in both TG AD mouse models (Trinchese et al., 2004; Delatour et al., 2006; Oberg et al., in press) and human AD patients (Braak and Braak, 1991). Reduced volumes were also noted in the olfactory bulb and piriform cortex of TG mice. This finding is supported by previous observations of olfactory dysfunction in AD patients (Thompson et al., 1998; Attems et al., 2005), and in the Tg2576 APP mouse model of AD (Smith et al., 2007). Several white matter tracts, particularly the anterior commissure, corpus callosum, internal capsule, and dorsal hippocampal commissure, also showed localized reductions in size in TG mice relative to their WT counterparts. Developmental abnormalities in the fiber connections may help to interpret the anatomical underpinnings of cognitive impairment in the studied TG model (Howlett et al., 2004; Trinchese et al., 2004). Volume reduction was also observed in the cerebellar paraflocculus and regions of the cerebellar commissure in the TG group. While the cerebellum generally remains unaffected in AD patients, the development of AD pathology in the cerebellum has been reported in early-onset patients with PS1 mutations (Larner and Doran, 2006).

Several neuroanatomical regions demonstrated volume expansion in TG mice, such as the lateral and third ventricles. Enlargement of these particular regions has been observed in volumetric studies of this transgenic murine model (Delatour et al., 2006; Oberg et al., in press). In brain parenchyma, the bed nuclei of the stria terminalis, as well as the dorsal superior colliculus and periaqueductal gray of the brain stem, also demonstrated relative enlargement in the TG group. Interestingly, hypertrophy of the bed nuclei has been observed in studies of late-stage AD patients due to enlargement of galanin-containing fibres within the cholinergic basal forebrain (Mufson et al., 1993), while extensive plaque deposition in the brain stem has also been previously reported (Iseki et al., 1989).

By examining the interaction term between genotype and age, we were able to elucidate regions with differences in aging between TG and WT groups. As previously mentioned, these dynamic effects are dependent on both the local value of the age and genotype terms and, therefore, must be interpreted on a region-by-region basis. For example, a significant positive effect was observed in a focal portion of the left entorhinal cortex in WT versus TG. Detailed examination revealed relative volume growth with age in WT mice, while no change was detected in the same region of TG animals (Fig. 4a). Regions within the retrosplenial granular cortex, ventrolateral hippocampus, and flocculus demonstrated age-related growth in WT mice, while we observed volumetric decline, in TG mice. With the exception of the flocculus, these regions are all known to be affected in the progression of disease in humans (Braak and Braak, 1991; Lerch et al., 2005) and mouse models of AD (Hsia et al., 1999; Reilly et al., 2003; Palop et al., 2005).

The primary somatosensory, retrosplenial, cingulate, and piriform cortical regions exhibited smaller baseline volumes in the TG mice compared to WT mice, but were shown to increase in volume over the age range studied. This finding suggests that a process of delayed development had occurred and concurs with the hypothesis proposed by Delatour et al. (Delatour et al., 2006) describing a process of interrupted normal growth in TG mice in certain brain regions. Given that the mutant APP transgene is constitutively expressed, it is not surprising that phenotypic differences are evident at a young age.

Interestingly, there was a lack of general atrophy in TG mice relative to their WT littermates aside from a few very focal regions within the dorsolateral hippocampus, retrosplenial cortex, and cerebellum. Instead, most of the anatomical differences appeared to result from a developmental, rather than a degenerative, process. These results, of course, require rigorous correlation with microscopic/molecular studies to better understand the neuropathological changes underlying these gross morphological changes.

In this study, mixed-effects analysis was limited to the application of a single statistical model across all brain voxels. Based on the plots of individual trajectories in Figs. 3 and 4, it is apparent that a linear model may not be optimal for all cases. However, given the relatively small sample size of this study, we have been cautious in model selection in order to avoid over-interpreting the data using insufficiently powered higher-order models. Future studies with larger sample sizes and the inclusion of later timepoints may employ modeling with higher-order, curvilinear components. For example, a step-down model selection algorithm, where each voxel would be fit with the polynomial mixed-effects model that best explains the variance, may allow for more detailed characterization of developmental trajectories (Shaw et al., 2007). We originally tested for main effects of gender, as well as interactions of gender with age and genotype. However, the inclusion of these terms did not result in any significant effects in the analysis. These terms were, therefore, removed in favour of a simpler model omitting gender as a covariate (see Eq. (4)). While gender-related dimorphisms in murine neuroanatomy have previously been reported using DBM (Spring et al., 2007), this study used *ex vivo* images with a 32 μm isotropic resolution. At this high spatial resolution, regional analyses were able to reveal distortions/movements between 30-180 μm. Given the lower resolution of our *in vivo* scans (156 μm isotropic), it is unlikely that the subtle effects of gender would influence our data, a conclusion which is supported by the lack of any significant effects of gender in our analysis.

In summary, our results support the utility of longitudinal DBM for the study of *in vivo* multiple timepoint datasets involving mouse models of AD in an automated and exploratory fashion. We were able to identify interesting growth differences between transgenic APP/PS1 AD mice and their wild-type littermates with strong, supporting pathophysiological interpretations. The seamless combination of morphological data obtained from this technique with complementary studies including functional MRI (fMRI), positron emission tomography (PET), quantitative immunohistochemistry, as well as cognitive performance testing, should allow for an improved understanding of complex neuropathological changes and their consequences in multiple diseases of the central nervous system.

Acknowledgments

The authors would like to thank Drs. Tomas Klason and Fu-Hua Wang at the MR Center of AstraZeneca R&D (AstraZeneca, Södertälje, Sweden) for kindly supplying the MRI and manual segmentation datasets, and Dr. Claude Lepage for valuable discussions regarding the automated image processing pipeline. This work was supported by funds from the Montreal Neurological Institute (B.J.B.). B.J.B. is a Killam Scholar at the Montreal Neurological Institute. J.P.L. is supported by the Canadian Institutes for Health Research. The Mouse Imaging Centre (MICe) acknowledges funding from the Canada Foundation for Innovation and the Ontario Innovation Trust for providing facilities along with The Hospital for Sick Children, as well as operating funds from the Burroughs Wellcome Fund, the Canadian Institutes of Health Research, the National Cancer Institute of Canada - Terry Fox Program Projects, the National Institutes of Health and the Ontario Research and Development Challenge Fund. R.M.H. holds a Canada Research Chair in Imaging.

References

Anderson, V.C., Litvack, Z.N., Kaye, J.A., 2005. Magnetic resonance approaches to brain aging and Alzheimer disease-associated neuropathology. Top. Magn. Reson. Imaging 16 (6), 439–452.

Ashburner, J., Friston, K.J., 2000. Voxel-based morphometry—the methods. NeuroImage 11 (6 Pt 1), 805–821.

Ashburner, J., Friston, K.J., 2001. Why voxel-based morphometry should be used. NeuroImage 14 (6), 1238–1243.

Ashburner, J., Hutton, C., Frackowiak, R., Johnsrude, I., Price, C., Friston, K., 1998. Identifying global anatomical differences: deformation-based morphometry. Hum. Brain Mapp. 6 (5-6), 348–357.

Ashburner, J., Csernansky, J.G., Davatzikos, C., Fox, N.C., Frisoni, G.B., Thompson, P.M., 2003. Computer-assisted imaging to assess brain structure in healthy and diseased brains. Lancet Neurol. 2 (2), 79–88.

Attems, J., Lintner, F., Jellinger, K.A., 2005. Olfactory involvement in aging and Alzheimer's disease: an autopsy study. J. Alzheimers Dis. 7 (2), 149–157.

Aucoin, J.S., Jiang, P., Aznavour, N., Tong, X.K., Buttini, M., Descarries, L., Hamel, E., 2005. Selective cholinergic denervation, independent from oxidative stress, in a mouse model of Alzheimer's disease. Neuroscience 132 (1), 73–86.

Barnes, J., Foster, J., Fox, N.C., 2007. Structural magnetic resonance imaging-derived biomarkers for Alzheimer's disease. Biomarkers Med. 1 (1), 79–92.

Bookstein, F.L., 1997. Landmark methods for forms without landmarks: morphometrics of group differences in outline shape. Med. Image Anal. 1 (3), 225–243.

Bookstein, F.L., 2001. Voxel-based morphometry should not be used with imperfectly registered images. NeuroImage 14 (6), 1454–1462.

Braak, H., Braak, E., 1991. Neuropathological stageing of Alzheimer-related changes. Acta Neuropathol. (Berl) 82 (4), 239–259.

Cao, J., Worsley, K.J., 1999. The detection of local shape changes via the geometry of Hotelling's T^2 fields. Ann. Stat. 27 (3), 925–942.

Chen, X.J., Kovacevic, N., Lobaugh, N.J., Sled, J.G., Henkelman, R.M., Henderson, J.T., 2006. Neuroanatomical differences between mouse strains as shown by high-resolution 3D MRI. NeuroImage 29 (1), 99–105.

Chung, M.K., Worsley, K.J., Paus, T., Cherif, C., Collins, D.L., Giedd, J.N., Rapoport, J.L., Evans, A.C., 2001. A unified statistical approach to deformation-based morphometry. NeuroImage 14 (3), 595–606.

Collins, D.L., Neelin, P., Peters, T.M., Evans, A.C., 1994. Automatic 3D intersubject registration of MR volumetric data in standardized Talairach space. J. Comput. Assist. Tomogr. 18 (2), 192–205.

Collins, D.L., Holmes, C.J., Peters, T.M., Evans, A.C., 1995. Automatic 3-D model-based neuroanatomical segmentation. Hum. Brain Mapp. 3 (3), 190–208.

Davatzikos, C., Vaillant, M., Resnick, S.M., Prince, J.L., Letovsky, S., Bryan, R.N., 1996. A computerized approach for morphological analysis of the corpus callosum. J. Comput. Assist. Tomogr. 20 (1), 88–97.

Delatour, B., Guegan, M., Volk, A., Dhenain, M., 2006. In vivo MRI and histological evaluation of brain atrophy in APP/PS1 transgenic mice. Neurobiol. Aging 27 (6), 835–847.

Fox, N.C., Crum, W.R., Scahill, R.I., Stevens, J.M., Janssen, J.C., Rossor, M.N., 2001. Imaging of onset and progression of Alzheimer's disease with voxel-compression mapping of serial magnetic resonance images. Lancet 358 (9277), 201–205.

Genovese, C.R., Lazar, N.A., Nichols, T., 2002. Thresholding of statistical maps in functional neuroimaging using the false discovery rate. NeuroImage 15 (4), 870–878.

Good, C.D., Johnsrude, I.S., Ashburner, J., Henson, R.N., Friston, K.J., Frackowiak, R.S., 2001. A voxel-based morphometric study of ageing in 465 normal adult human brains. NeuroImage 14 (1 Pt 1), 21–36.

Hebert, L.E., Scherr, P.A., Bienias, J.L., Bennett, D.A., Evans, D.A., 2003. Alzheimer disease in the US population: prevalence estimates using the 2000 census. Arch. Neurol. 60 (8), 1119–1122.

Howlett, D.R., Richardson, J.C., Austin, A., Parsons, A.A., Bate, S.T., Davies, C.D., Gonzalez, I.M., 2004. Cognitive correlates of a[beta] deposition in male and female mice bearing amyloid precursor protein and presenilin-1 mutant transgenes. Brain Res. 1017 (1-2), 130–136.

Hsia, A.Y., Masliah, E., Mcconlogue, L., Yu, G.Q., Tatsuno, G., Hu, K., Kholodenko, D., Malenka, R.C., Nicoll, R.A., Mucke, L., 1999. Plaque-independent disruption of neural circuits in Alzheimer's disease mouse models. Proc. Natl. Acad. Sci. U. S. A 96 (6), 3228–3233.

Iseki, E., Matsushita, M., Kosaka, K., Kondo, H., Ishii, T., Amano, N., 1989. Distribution and morphology of brain stem plaques in Alzheimer's disease. Acta Neuropathol. (Berl) 78 (2), 131–136.

Janke, A.L., de Zubicaray, G., Rose, S.E., Griffin, M., Chalk, J.B., Galloway, G.J., 2001. 4D deformation modeling of cortical disease progression in Alzheimer's dementia. Magn. Reson. Med. 46 (4), 661–666.

Kovacevic, N., Henderson, J.T., Chan, E., Lifshitz, N., Bishop, J., Evans, A.C., Henkelman, R.M., Chen, X.J., 2005. A three-dimensional MRI atlas of the mouse brain with estimates of the average and variability. Cereb. Cortex 15 (5), 639–645.

Larner, A.J., Doran, M., 2006. Clinical phenotypic heterogeneity of Alzheimer's disease associated with mutations of the presenilin-1 gene. J. Neurol. 253 (2), 139–158.

Larson, J., Lynch, G., Games, D., Seubert, P., 1999. Alterations in synaptic transmission and long-term potentiation in hippocampal slices from young and aged PDAPP mice. Brain Res. 840 (1-2), 23–35.

Lavebratt, C., Trifunovski, A., Persson, A.S., Wang, F.H., Klason, T., Ohman, I., Josephsson, A., Olson, L., Spenger, C., Schalling, M., 2006. Carbamazepine protects against megencephaly and abnormal expression of BDNF and Nogo signaling components in the mceph/mceph mouse. Neurobiol. Dis. 24 (2), 374–383.

Leow, A.D., Klunder, A.D., Jack, C.R., Toga, A.W., Dale, A.M., Bernstein, M.A., Britson, P.J., Gunter, J.L., Ward, C.P., Whitwell, J.L., Borowski, B.J., Fleisher, A.S., Fox, N.C., Harvey, D., Kornak, J., Schuff, N., Studholme, C., Alexander, G.E., Weiner, M.W., Thompson, P.M., 2006. Longitudinal stability of MRI for mapping brain change using tensor-based morphometry. NeuroImage 31 (2), 627–640.

Lerch, J.P., Pruessner, J.C., Zijdenbos, A., Hampel, H., Teipel, S.J., Evans, A.C., 2005. Focal decline of cortical thickness in Alzheimer's disease identified by computational neuroanatomy. Cereb. Cortex 15 (7), 995–1001.

Mucke, L., Masliah, E., Yu, G.-Q., Mallory, M., Rockenstein, E.M., Tatsuno, G., Hu, K., Kholodenko, D., Johnson-Wood, K., Mcconlogue, L., 2000. High-level neuronal expression of abeta 1-42 in wild-type human amyloid protein precursor transgenic mice: Synaptotoxicity without plaque formation. J. Neurosci. 20 (11), 4050–4058.

Mufson, E.J., Cochran, E., Benzing, W., Kordower, J.H., 1993. Galaninergic innervation of the cholinergic vertical limb of the diagonal band (Ch2) and bed nucleus of the stria terminalis in aging, Alzheimer's disease and Down's syndrome. Dementia 4 (5), 237–250.

Nieman, B.J., Flenniken, A.M., Adamson, S.L., Henkelman, R.M., Sled, J.G., 2006. Anatomical phenotyping in the brain and skull of a mutant mouse by magnetic resonance imaging and computed tomography. Physiol. Genomics 24 (2), 154–162.

Niwa, K., Kazama, K., Younkin, S.G., Carlson, G.A., Iadecola, C., 2002. Alterations in cerebral blood flow and glucose utilization in mice overexpressing the amyloid precursor protein. Neurobiol. Dis. 9 (1), 61–68.

Oberg, J., Spenger, C., Wang, F.-H.H., Andersson, A., Westman, E., Skoglund, P., Sunnemark, D., Norinder, U., Klason, T., Wahlund, L.-O.O., Lindberg, M., in press. Age related changes in brain metabolites observed by (1)H MRS in APP/PS1 mice. Neurobiol Aging.

Palop, J.J., Chin, J., Bien-Ly, N., Massaro, C., Yeung, B.Z., Yu, G.Q., Mucke, L., 2005. Vulnerability of dentate granule cells to disruption of arc expression in human amyloid precursor protein transgenic mice. J. Neurosci. 25 (42), 9686–9693.

Palop, J.J., Jones, B., Kekonius, L., Chin, J., Yu, G.Q., Raber, J., Masliah, E., Mucke, L., 2003. Neuronal depletion of calcium-dependent proteins in the dentate gyrus is tightly linked to Alzheimer's disease-related cognitive deficits. Proc. Natl. Acad. Sci. U. S. A. 100 (16), 9572–9577.

Paxinos, G., Franklin, K.B.J., 2001. The Mouse Brain in Stereotaxic Coordinates, Second Edition. Academic Press.

Pinheiro, J.C., Bates, D.M., 2002. Mixed Effects Models in S and S-Plus. Springer.

Redwine, J.M., Kosofsky, B., Jacobs, R.E., Games, D., Reilly, J.F., Morrison, J.H., Young, W.G., Bloom, F.E., 2003. Dentate gyrus volume is reduced before onset of plaque formation in PDAPP mice: a magnetic resonance microscopy and stereologic analysis. Proc. Natl. Acad. Sci. U. S. A. 100 (3), 1381–1386.

Reilly, J.F., Games, D., Rydel, R.E., Freedman, S., Schenk, D., Young, W.G., Morrison, J.H., Bloom, F.E., 2003. Amyloid deposition in the hippocampus and entorhinal cortex: Quantitative analysis of a transgenic mouse model. Proc. Natl. Acad. Sci. U. S. A. 100 (8), 4837–4842.

Shaw, P., Eckstrand, K., Sharp, W., Blumenthal, J., Lerch, J.P., Greenstein, D., Clasen, L., Evans, A., Giedd, J., Rapoport, J.L., 2007. From the Cover: Attention-deficit/hyperactivity disorder is characterized by a delay in cortical maturation. Proc. Natl. Acad. Sci. U. S. A. 104 (49), 19649–19654.

Sled, J.G., Zijdenbos, A.P., Evans, A.C., 1998. A nonparametric method for automatic correction of intensity nonuniformity in MRI data. IEEE Trans. Med. Imag. 17 (1), 87–97.

Smith, K.D., Kallhoff, V., Zheng, H., Pautler, R.G., 2007. In vivo axonal transport rates decrease in a mouse model of Alzheimer's disease. NeuroImage 35 (4), 1401–1408.

Spring, S., Lerch, J.P., Henkelman, R.M., 2007. Sexual dimorphism revealed in the structure of the mouse brain using three-dimensional magnetic resonance imaging. NeuroImage 35 (4), 1424–1433.

Studholme, C., Cardenas, V., Maudsley, A., Weiner, M., 2003. An intensity consistent filtering approach to the analysis of deformation tensor derived maps of brain shape. NeuroImage 19 (4), 1638–1649.

Studholme, C., Cardenas, V., Blumenfeld, R., Schuff, N., Rosen, H.J., Miller, B., Weiner, M., 2004. Deformation tensor morphometry of semantic dementia with quantitative validation. NeuroImage 21 (4), 1387–1398.

Thompson, P.M., Toga, A.W., 1997. Detection, visualization and animation of abnormal anatomic structure with a deformable probabilistic brain atlas based on random vector field transformations. Med. Image Anal. 1 (4), 271–294.

Thompson, M.D., Knee, K., Golden, C.J., 1998. Olfaction in persons with Alzheimer's disease. Neuropsychol. Rev. 8 (1), 11–23.

Thompson, P.M., Hayashi, K.M., Dutton, R.A., Chiang, M.C., Leow, A.D., Sowell, E.R., De Zubicaray, G., Becker, J.T., Lopez, O.L., Aizenstein, H.J., Toga, A.W., 2007. Tracking Alzheimer's disease. Ann. N.Y. Acad. Sci. 1097, 183–214.

Trinchese, F., Liu, S., Battaglia, F., Walter, S., Mathews, P.M., Arancio, O., 2004. Progressive age-related development of Alzheimer-like pathology in APP/PS1 mice. Ann. Neurol. 55 (6), 801–814.

Verma, R., Mori, S., Shen, D., Yarowsky, P., Zhang, J., Davatzikos, C., 2005. Spatiotemporal maturation patterns of murine brain quantified by diffusion tensor MRI and deformation-based morphometry. Proc. Natl. Acad. Sci. U. S. A. 102 (19), 6978–6983.

Zhang, J., Chen, Y.-B., Hardwick, M.J., Miller, M.I., Plachez, C., Richards, L.J., Yarowsky, P., van Zijl, P., Mori, S., 2005. Magnetic resonance diffusion tensor microimaging reveals a role for Bcl-x in brain development and homeostasis. J. Neurosci. 25 (8), 1881–1888.